PHYSICAL REVIEW E **88**, 053005 (2013)

Steady and transient thin-jet flow of a viscoelastic fluid

Michael A. Hanyk and Roger E. Khayat[*]
Department of Mechanical and Materials Engineering, The University of Western Ontario, London, Ontario, Canada

(Received 19 August 2012; revised manuscript received 15 July 2013; published 7 November 2013)

Steady and transient two-dimensional thin-jet flow of a viscoelastic is examined theoretically. The influence of inertia, elasticity, and gravity is emphasized. The fluid is assumed to emerge from a vertical channel and to be driven by a pressure gradient and/or gravity. The boundary-layer equations are generalized for a viscoelastic thin film obeying the Oldroyd-B constitutive model. In contrast to the commonly used depth-averaging solution method, the strong nonlinearities are preserved in the present formulation as the viscoelastic boundary-layer equations are solved by expanding the flow field in terms of orthonormal shape functions. It is found that elasticity and gravity have the most profound effect on the steady state as well as the transient behavior of the viscoelastic film. The initial conditions strongly determine the stability of the film, which for all transient cases examined were shown to be stable despite the presence of initial instabilities.

DOI: 10.1103/PhysRevE.88.053005 PACS number(s): 47.50.Cd, 47.15.gm

I. INTRODUCTION

This study examines theoretically the steady and transient flow of a viscoelastic fluid free-surface jet emerging from a vertical channel. The focus of related studies has mainly been on steady jet flow since it is the long-term behavior of the flow, after transient effects have subsided, that is generally important in polymer processing. In contrast, when irregularity and instability occur, it is usually the initial stages of development, long before the flow may (or may not) reach steady state, which can be traced to the origin of the instability. The time taken for a fluid to reach steady state is also of importance. Because polymeric fluids exhibit different relaxation times, they will therefore display a different transient response.

The present study examines the intricate interplay between inertia and viscoelastic effects in the presence of gravity, which is of fundamental importance given the significant qualitative role that elasticity plays in this case. In general, inertia has been neglected in most of the studies on viscoelastic jets since polymeric liquids behave like creeping flow in practice. However, there are applications such as fiber spinning [1], film casting [2] and high-speed extrusions [3] in which inertia is significant. Shah and Pearson [4] showed that inertia plays an important role in fiber spinning as it enhances flow stability. Inertia becomes particularly important in modern high-speed film casting [2], and coating [5] flows. The stabilizing role of inertia was also demonstrated experimentally in film casting and fiber spinning by Seyfzadeh *et al.* [6], and Doufas and McHugh [7], respectively, suggesting that inertia affects the stability region of these processes.

The literature abounds with modeling and simulation studies on laminar Newtonian jet flow (see, for instance, Chang [8] for a review), and, to a much lesser extent, on non-Newtonian jet flow. Berdaudo *et al.* [9] examined the free-surface flow of a viscoelastic fluid emerging from various geometries. Their work focused on the die-swell phenomenon, preceded by confined convergent two-dimensional and axisymmetric geometries, using the finite-element method, and neglecting inertia. Therein, a summery of computational studies can be found. Kang and Chen [10] studied creeping gravity-driven non-Newtonian films in the presence of the surface tension effect. Using a boundary-layer (BL) or thin-film approach, Tome *et al.* [11] examined the transient die swell and buckling of planar jets for Newtonian and generalized Newtonian fluids. Surface tension jet breakup of non-Newtonian fluids has also been examined, both experimentally by Christanti and Walker [12] and theoretically by Bousfield *et al.* [13]. The transient response resulting from the spreading of surfactant on a thin weakly viscoelastic film was also examined theoretically by Zhang *et al.* [14].

For viscoelastic jets, the main focus in the literature has been on die swell for creeping flow. Tieu and Joseph [15] considered surface tension driven flow, and Tran-Cong and Phan-Thien [16] examined the creeping flow extrusion of a viscoelastic fluid from triangular and square dies. The importance of gravity was demonstrated by Liang *et al.* [17], who carried out flow visualization and measurement for steady viscoelastic jet issuing from a capillary and from an orifice under gravity. Their experiments revealed that, depending upon the elasticity level of the fluid, the jet width may increase, decrease, or remain unchanged downstream, at least within a certain distance from the exit. In this case, the interplay between gravity and elasticity dictates the jet behavior. In their experiments, Middleman and Gavis [18] observed that the viscoelastic jet expands for low ejection velocities. The expansion reaches a maximum with increasing flow rate. However, the expansion begins to weaken as the flow rate is increased further, and the viscoelastic jet ultimately contracts when inertia becomes significant. In their study, however, they used only a power-law model to represent the fluid properties, which does not allow a direct quantitative comparison with the results of the present study. A similar interplay between inertia and elasticity is also responsible for the delayed die swell phenomenon, which appears to be caused by some inertial mechanism related to the change in flow type from subcritical to supercritical [19]. Delayed swell was captured theoretically in a recent study by Saffari and Khayat [20] using the method of matched asymptotic expansions for the flow near channel exit.

Generally, the numerical treatment of transient free-surface flow remains challenging. The problems associated with frequent remeshing and mesh resizing required for the rapid

---

[*] Corresponding author: rkhayat@uwo.ca

spatiotemporal variations in the flow field can make unsuitable conventional solutions schemes such as finite-element and/or difference methods. The flow of a thin film is commonly described using a BL approach. Typically, an *ad hoc* simplification of the BL solution is achieved using a self-similar parabolic flow profile [21,22]. This amounts to depth-averaging the BL equations, which, in the limit of creeping flow of a Newtonian fluid, leads to an exact formulation. The self-similar behavior is not expected to hold in the presence of high inertia or strong normal stress effects. The solution of the BL equations remains essentially as difficult to obtain as that of the Navier-Stokes equations for a Newtonian film [23]. The depth-averaging method leads to a second-order accurate solution in time, yielding plausible results, but raises doubt in the presence of strong convective (and upper convective) nonlinearities due to the semiparabolic assumption [23,24]. The numerical computation of viscoelastic fluid jets presents additional difficulties, which are usually due to the lack of convergence and stability of the complex numerical scheme handling nonlinearities of inertial, elastic, and geometrical nature. The hybrid type of governing equations (elliptic and/or hyperbolic), geometrical singularities such as reentrant corner or die induced stress singularities, add to the numerical challenges.

Using a spectral approach, Khayat and co-workers examined extensively highly nonlinear flows, in the presence of inertia and elasticity, of thin films over rigid substrates of arbitrary shape. The planar flow of a Newtonian film was considered over stationary [25,26] and moving [27] substrates. The coating of shear-thinning [28] and viscoelastic [29] fluids were examined for a planar substrate as well as an axisymmetric substrate [30]. In the present study, the same spectral approach is adapted to a generalized thin-film formulation for a free-surface jet. The system is first mapped onto a rectangular domain, followed by the expansion of the velocity field in terms of orthonormal basis functions. The Galerkin projection is used to derive the equations that govern the coefficients of expansion, which are then integrated numerically. This formulation is similar to the one adopted by Khayat and Kim [30] for viscoelastic coating flow, and by German and Khayat [5] for thin-jet flow of a Newtonian fluid. Unlike the depth-averaging method, the spectral methodology proposed becomes particularly suited for the early onset of wave propagation near the channel exit in the presence of strong normal-stress effect.

II. PROBLEM FORMULATION AND SOLUTION PROCEDURE

In this section, the governing equations are introduced, including the scaled conservation and constitutive equations, as well as the boundary and initial conditions for a viscoelastic thin fluid jet. Also included in this section is the solution procedure.

A. Governing equations, boundary, and initial conditions

The fluid examined in this study is assumed to be an incompressible polymeric solution represented by a single relaxation time and constant viscosity. The fluid properties include the density ρ, viscosity μ, surface tension coefficient σ, and relaxation time λ. The solution viscosity $\mu = \mu_s + \mu_p$ comprises the Newtonian solvent viscosity μ_s and polymeric solute viscosity μ_p. Regardless of the nature of the fluid, the continuity and momentum conservation equations must hold. For an incompressible fluid, the conservation equations are

$$\nabla\cdot\mathbf{U}=0,\quad \rho(\mathbf{U}_{,T}+\mathbf{U}\cdot\nabla\mathbf{U})=\nabla\cdot\mathbf{\Sigma}+\rho\mathbf{g}, \tag{2.1}$$

where $\mathbf{U}$ is the velocity vector, $\mathbf{g}$ is the gravitational acceleration, T is time, ∇ is the gradient operator, and $\mathbf{\Sigma}$ is the stress tensor. A subscript following a comma denotes partial differentiation. There are two components making up the deviatoric part of the stress tensor, a Newtonian constituent (solvent), and a polymeric constituent (solute) $\mathbf{T}$. The stress tensor is then expressed as

$$\mathbf{\Sigma}=-P\mathbf{I}+\mu_s(\nabla\mathbf{U}+\nabla\mathbf{U}^T)+\mathbf{T}, \tag{2.2}$$

where P is the hydrostatic pressure, and T denotes matrix transposition. The polymeric constitutive equation for $\mathbf{T}$ is taken to correspond to an Oldroyd-B fluid and is written in the form [31]

$$\begin{aligned}\lambda(\mathbf{T}_{,T}+\mathbf{U}\cdot\nabla\mathbf{T}-\mathbf{T}\cdot\nabla\mathbf{U}-\nabla\mathbf{U}^T\cdot\mathbf{T})+\mathbf{T}\\ =\mu_p(\nabla\mathbf{U}+\nabla\mathbf{U}^T).\end{aligned} \tag{2.3}$$

The equation for a Maxwell fluid is recovered in the limit $\mu_s \to 0$ in Eqs. (2.1)–(2.3), and the limit $\mu \to \mu_s$ leads to the Navier-Stokes equations. The problem is now examined using a Cartesian coordinates in the plane.

The flow of the viscoelastic jet emerging from a channel is schematically depicted in Fig. 1 in the (X, Z) plane. The X axis is a line of symmetry and lies in the vertical (streamwise) direction, and the Z axis is in the horizontal (transverse) direction. The domain of the fluid is represented by $\Omega(X, Z, T)$, with the (half) jet thickness denoted by $Z = H(X, T)$. The channel exit coincides with $X = 0$, and the (symmetric) flow is examined in the (X, Z) plane, with $Z = 0$ corresponding to the line of symmetry. The flow is induced by either a pressure gradient inside the channel and/or gravity, but for this study, the emphasis will be on pressure-driven flow. The streamwise and transverse scale lengths are chosen to be the length of

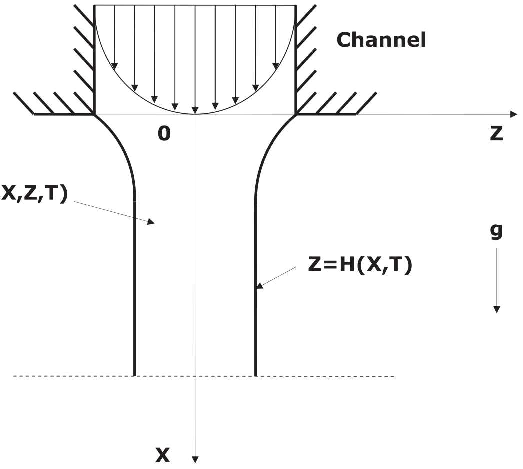

FIG. 1. Schematic illustration of two-dimensional jet flow emerging from a vertical channel.

the jet L and the channel half width H_0 respectively. For both Newtonian and non-Newtonian thin films, there are four main dimensionless parameters. These are, namely, the aspect ratio ε, the Reynolds number Re, the Froude number Fr, and the capillary number Ca. Explicitly written, these take the following form:

$$\varepsilon = \frac{H_0}{L}, \quad \mathrm{Re} = \varepsilon \frac{\rho U_0 H_0}{\mu}, \quad \mathrm{Fr} = \frac{U_0}{\sqrt{gL}}, \quad \mathrm{Ca} = \frac{\mu U_0}{\sigma}, \tag{2.4}$$

where the mean velocity in the channel in the absence of gravity U_0 is taken as the reference velocity. Additional to these parameters are the similarity parameters for a viscoelastic fluid, which include the Deborah number De, the solvent-to-solute viscosity ratio Rv, and the solvent-to-solution viscosity ratio a:

$$\mathrm{De} = \frac{\lambda U_0}{L}, \quad \mathrm{Rv} = \frac{\mu_s}{\mu_p}, \quad a = \frac{\mu_p}{\mu} = \frac{1}{\mathrm{Rv}+1}. \tag{2.5}$$

In this study, the fluid film is assumed thin, with $\varepsilon \ll 1$. Thus, ε is taken as the perturbation parameter in order to reduce the formulation to that of the boundary-layer type. The scaling of the velocity vector (U, W), pressure P, position coordinates (X, Z), and time T is the same as for a Newtonian thin layer, leading to the following nondimensional variables:

$$x = \frac{X}{L}, \quad z = \frac{Z}{H_0}, \quad t = \frac{U_0}{L}T, \quad u = \frac{U}{U_0}, \quad w = \frac{W}{\varepsilon U_0}, \quad h = \frac{H}{H_0}, \quad p = \frac{L\varepsilon^2}{\mu U_0}P. \tag{2.6a}$$

As to the polymeric normal and shear stress components (T_{XX},T_{ZZ},$T_{XZ} = T_{ZX}$), one may generally set

$$\tau_{xx} = \frac{L\varepsilon^{\alpha}}{\mu U_0}T_{XX}, \quad \tau_{zz} = \frac{L\varepsilon^{\gamma}}{\mu U_0}T_{ZZ}, \quad \tau_{xz}\,(\tau_{zx}) = \frac{L\varepsilon^{\beta}}{\mu U_0}T_{XZ}\,(T_{ZX}). \tag{2.6b}$$

Note that the stress tensor is symmetric. The constants, α, β, γ are determined by ensuring that the terms in the conservation and constitutive equations balance. Similarly to Newtonian flow, the thin-film or boundary-layer equations are derived from the dimensionless form of conservation and constitutive equations (2.1)–(2.3), excluding terms of $O(\varepsilon^2)$ and higher. In this case, the equations reduce to

$$u_{,x} + w_{,z} = 0, \tag{2.7a}$$

$$\mathrm{Re}(u_{,t} + uu_{,x} + wu_{,z}) = -p_{,x} + a\mathrm{Rv}\,u_{,zz} + \varepsilon^{2-\alpha}\tau_{xx,x} + \varepsilon^{1-\beta}\tau_{xz,z} + \frac{\mathrm{Re}}{\mathrm{Fr}^2}, \tag{2.7b}$$

$$p_{,z} = \varepsilon^{2-\gamma}\tau_{zz,z} + \varepsilon^{3-\beta}\tau_{xz,x}, \tag{2.7c}$$

$$\mathrm{De}[\varepsilon^{-\alpha}(\tau_{xx,t} + u\tau_{xx,x} + w\tau_{xx,z} - 2\tau_{xx}u_{,x}) - 2\varepsilon^{-1-\beta}\tau_{xz}u_{,z}] + \varepsilon^{-\alpha}\tau_{xx} = au_{,x}, \tag{2.7d}$$

$$\mathrm{De}[\varepsilon^{-\beta}(\tau_{xz,t} + u\tau_{xz,x} + w\tau_{xz,z}) - \varepsilon^{1-\alpha}\tau_{xx}w_{,x} - \varepsilon^{-1-\gamma}\tau_{zz}u_{,z}] + \varepsilon^{-\beta}\tau_{xz} = a\varepsilon^{-1}u_{,z}, \tag{2.7e}$$

$$\mathrm{De}[\varepsilon^{-\gamma}(\tau_{zz,t} + u\tau_{zz,x} + w\tau_{zz,z} - 2\tau_{zz}w_{,z}) - 2\varepsilon^{1-\beta}\tau_{xz}w_{,x}] + \varepsilon^{-\gamma}\tau_{zz} = 2aw_{,z}. \tag{2.7f}$$

In order to ensure proper coupling between velocity and stress, the polymeric stress terms (similarly to the pressure gradient term in the Newtonian BL formulation) must survive in the x-momentum equation (2.7a). In this case, the exponents α and β should be set equal to 2 and 1, respectively. Consequently, this ensures the survival of all the terms in the normal stress equation (2.7d) for τ_{XX}. This results in the streamwise normal stress component τ_{XX} not to depend strongly on the streamwise elongation term $u_{,X}$, which should be the case for a shear dominated (boundary-layer) flow. However, this stress component remains significant due to the nonlinear coupling with shear effects. With α and β set, the survival of the terms in the shear stress equation (2.7e) for τ_{XZ} and normal stress equation (2.7f) for τ_{ZZ} can be achieved by setting $\gamma = 0$. The z-momentum equation (2.7c) now shows that $p_{,z} \sim O(\varepsilon^2)$. This demonstrates that the pressure gradient in the transverse direction is negligible, which is consistent with the limit of a Newtonian jet flow. Hence, assuming no body forces exist in the transverse direction, the pressure is a function of the streamwise direction and time only. The conservation and constitutive equations reduce to

$$u_{,x} + w_{,z} = 0, \tag{2.8a}$$

$$\mathrm{Re}(u_{,t} + uu_{,x} + wu_{,z}) = -p_{,x} + a\mathrm{Rv}\,u_{,zz} + \tau_{xx,x} + \tau_{xz,z} + \frac{\mathrm{Re}}{\mathrm{Fr}^2}, \tag{2.8b}$$

$$\mathrm{De}(\tau_{xx,t} + u\tau_{xx,x} + w\tau_{xx,z} - 2\tau_{xz}u_{,z} - 2\tau_{xx}u_{,x}) + \tau_{xx} = 0, \tag{2.8c}$$

$$\mathrm{De}(\tau_{xz,t} + u\tau_{xz,x} + w\tau_{xz,z} - \tau_{xx}w_{,x} - \tau_{zz}u_{,z}) + \tau_{xz} = au_{,z}, \tag{2.8d}$$

$$\mathrm{De}(\tau_{zz,t} + u\tau_{zz,x} + w\tau_{zz,z} - 2\tau_{xz}w_{,x} - 2\tau_{zz}w_{,z}) + \tau_{zz} = 2aw_{,z}. \tag{2.8e}$$

These equations are exactly the same (with the addition of inertia, Newtonian solvent and gravity) as those derived by Renardy for BL flow of a Maxwell fluid [32]. It is emphasized that the scaling (2.6b) suggests that, for a thin film, not all stress components are of the same order of magnitude. Indeed, assuming $\mathrm{De} \simeq O(1)$ and neglecting terms of $O(\varepsilon)$ and higher, it is not difficult to show that, if the same stress scale is adopted in (2.6b), upon setting $\alpha = \beta = \gamma = 0$, then no polymeric stress contribution survives in the momentum equation (2.7b). In this case, Eq. (2.7d) indicates that $\tau_{xz} \simeq 0$, leading, in turn, to $\tau_{zz} \simeq \frac{a}{\mathrm{De}}$ from both (2.7e) and (2.7f). Clearly, this result is unacceptable except in the Newtonian limit ($a \rightarrow 0$). The streamwise normal stress component τ_{xx} remains undetermined to leading order in the BL formulation. Similarly, upon setting $\alpha = \beta = \gamma = 1$, adopting H_0 instead of L as length scale, yields $\tau_{zz} = \tau_{xz} \simeq 0$.

The equations above must be solved subject to the dynamic and kinematic conditions at the free surface, the symmetry conditions at $z = 0$, and the channel exit conditions at $x = 0$. The preceding scaling was applied to the dynamic condition in the normal and tangential directions, resulting in

$$a\mathrm{Rv}\,u_{,z}(x,z=h,t) + \tau_{xz}(x,z=h,t) = \tau_{xx}(x,z=h,t)h_{,x}(x,t), \tag{2.9a}$$

$$p(x,z=h,t) = -\frac{\varepsilon^3}{\mathrm{Ca}}. \tag{2.9b}$$

Clearly, surface tension effect is negligible if $\mathrm{Ca} \simeq O(\varepsilon^2)$ or larger. It will be argued later (see Sec. IV) that this is, indeed, the case for most polymeric liquids, and surface tension effect will be neglected from now on. In dimensionless form, the kinematic condition becomes

$$w(x,z=h,t) = h_{,t}(x,t) + u(x,z=h,t)h_{,x}(x,t). \tag{2.10}$$

The flow conditions at the channel exit correspond to the flow inside an infinite channel. Thus,

$$\begin{aligned} u(x=0,z,t) &= \frac{1}{2}\left(3+\frac{\mathrm{Re}}{\mathrm{Fr}^2}\right)(1-z^2),\\ w(x=0,z,t) &= 0,\\ \tau_{xx}(x=0,z,t) &= 2a\mathrm{De}\, z^2\left(3+\frac{\mathrm{Re}}{\mathrm{Fr}^2}\right)^2,\\ \tau_{xz}(x=0,z,t) &= -az\left(3+\frac{\mathrm{Re}}{\mathrm{Fr}^2}\right),\\ \tau_{zz}(x=0,z,t) &= 0. \end{aligned} \tag{2.11a}$$

The jet thickness at the channel exit is assumed fixed, so that

$$h(x=0,t) = 1. \tag{2.11b}$$

Finally, the symmetry conditions are:

$$w(x,z=0,t) = u_{,z}(x,z=0,t) = \tau_{xz}(x,z=0,t) = 0. \tag{2.12}$$

In this formulation it is assumed that no external force or pressure acts on the fluid surface. For a surface-pressure-driven flow the reader is referred to Kriegsmann *et al.* [33]. Also, since the pressure p does not depend on z, the pressure must vanish everywhere in order to satisfy the zero-pressure condition (2.9b). For this reason, the axial pressure gradient term of (2.8b) will no longer be included. The initial conditions for transient flow will be discussed later.

B. Solution procedure

Traditionally, for Newtonian thin-film flow, the equations are solved by imposing a semiparabolic profile for the velocity, and depth-averaging the equations across the thickness. The strong nonlinear effects originating from inertia and normal stress for a viscoelastic fluid make this approach unfeasible. The solution process is obviously difficult due to the explicit z dependence of the velocity and stress components. The formal handling of the transverse flow expansion is carried out similarly to past studies by Khayat and co-workers [25–30,34]. The spectral approach follows closely and generalizes the work of Zienkievicz and Heinrich [35] as the transverse velocity component is not neglected, and the change in surface height over time is included. The spectral methodology used has been extensively validated by Khayat and co-workers for the flow of thin jets and films. The validation is based on comparison with the finite-element solution and existing literature as well as assessment of higher-order modes, convergence and stability for inelastic [26–28,34] and viscoelastic [29,30] fluids. Only an outline of the solution procedure will be given next.

In order to apply the spectral approach, the flow domain is first mapped onto a rectangular domain. All flow variables are then expanded in terms of polynomial shape functions in the transverse direction. The Galerkin projection is then applied in order to generate the equations that determine the expansion coefficients. A Lagrangian time-stepping implicit finite-difference method is coupled with a fourth-order Runge-Kutta integration solution approach in the flow direction in order to determine the expansion coefficients. The present formulation is quite involved and will only be summarized in this paper. System (2.8) is reduced to a transient one-dimensional problem formulation by an expansion of the velocity and stress components in terms of orthonormal modes in the transverse direction. The following mapping is used:

$$\chi(x,z,t) = x, \quad \xi(x,z,t) = \frac{z}{h(x,t)}, \quad \tau(x,z,t) = t, \tag{2.13}$$

with $\xi \in [0, 1]$. The orthonormal shape functions $\phi_i(\xi)$, $\theta_i(\xi)$, $\psi_i(\xi)$ for the streamwise velocity u, normal stress component τ_{XX}, and shear component τ_{XZ} as well as the normal stress component τ_{ZZ} are shown as follows:

$$\begin{aligned} u(\chi,\xi,\tau) &= \sum_{i=1}^{M} U_i(\chi,\tau)\Phi_i(\xi),\\ \tau_{xx}(\chi,\xi,\tau) &= \sum_{i=1}^{M} Q_i(\chi,\tau)\theta_i(\xi),\\ \tau_{xz}(\chi,\xi,\tau) &= \sum_{i=1}^{M} S_i(\chi,\tau)\theta_i(\xi),\\ \tau_{zz}(\chi,\xi,\tau) &= \sum_{i=1}^{M} R_i(\chi,\tau)\psi_i(\xi), \end{aligned} \tag{2.14}$$

where M represents the number of modes and the unknown coefficients are $U_i(x,t)$, $Q_i(\chi,\tau)$, $S_i(\chi,\tau)$, and $R_i(\chi,\tau)$. In addition to the condition of orthonormality, the shape functions must also satisfy various boundary conditions. Some of these conditions are not obvious. One condition is the limit of Newtonian film flow being recovered for this viscoelastic formulation as $\mathrm{Rv} \to \infty$. One major difficulty for viscoelastic flow, as opposed to a Newtonian flow, is that the shear stress does not simply and necessarily vanish at the free surface. This becomes apparent when examining condition (2.9a), and also noting that there do not exist separate boundary conditions on shear and normal stresses. This, however, can be remedied by satisfying condition (2.9a) as well as recovering the Newtonian limit by simply setting the shear and normal stresses equal to zero at the free surface. Hence, assuming orthonormality, the following conditions apply for ϕ_i:

$$\langle \phi_i \phi_j \rangle = \delta_{ij}, \quad \phi_i'(\xi=0) = \phi_i'(\xi=1) = 0, \tag{2.15a}$$

which satisfy conditions (2.12). Here, δ_{ij} is the Kronecker δ, and $\langle\rangle$ denotes the integration over the interval $\xi \in [0, 1]$. Note that a prime denotes total differentiation. For θ_i, the normal and shear stress (τ_{XX}, τ_{XZ}) are taken to vanish at the free surface. In addition, to the symmetry conditions (2.12), it is not difficult to see that the vanishing of τ_{XX} at $z = 0$ is a condition that satisfies equation (2.8c). Thus,

$$\langle \theta_i \theta_j \rangle = \delta_{ij}, \quad \theta_i(\xi = 0) = \theta_i(\xi = 1) = 0. \qquad (2.15b)$$

The boundary conditions for Ψ_i are not as obvious. Nothing for certain can be said about τ_{zz} at either the free surface or line of symmetry. In this case, the corresponding shape function is assumed to satisfy only the condition of orthonormality, namely

$$\langle \psi_i \psi_j \rangle = \delta_{ij}. \qquad (2.15c)$$

Explicit form of the shape functions is given here for the first modes:

$$\phi_1(\xi) = 2\sqrt{\frac{35}{13}}\left(\xi^3 - \frac{3}{2}\xi^2\right), \quad \theta_1(\xi) = \sqrt{30}(\xi^2 - \xi), \qquad (2.16)$$
$$\psi_1(\xi) = 1.$$

The transverse velocity component, w, is determined by integrating the continuity equation (2.8a) to give

$$w(\chi,\xi,\tau) = \sum_{i=1}^{M} [h,_\chi(\xi\phi_i - \varphi_i)U_i - h\varphi_i U_{i,\chi}], \qquad (2.17)$$

where $\varphi_i(\xi) = \int_0^\xi \phi_i \, d\xi$. The insertion of expression (2.17) into the governing equations allows the elimination of w. Using expression (2.17), condition (2.10) becomes

$$h,_\tau + h \sum_{i=1}^{M} U_{i,\chi} \langle \phi_i \rangle + h,_\chi \sum_{i=1}^{M} U_i \langle \phi_i \rangle = 0. \qquad (2.18)$$

As long as the boundary and orthonormality conditions are satisfied, it is found that any number of arbitrary modes can be introduced. However, reasonable accuracy is achieved using $M > 3$. The expansion coefficients are obtained upon substitution of expansions (2.14) along with (2.17) and (2.18) into Eqs. (2.8). These equations are then multiplied by the appropriate shape function and integrated over the interval $\xi \in [0,1]$. This results in a system of $4M + 1$ partial differential equations in the (χ,τ) domain. These equations are then solved using a Lagrangian implicit finite-difference discretization scheme accompanied by a fourth-order Runge-Kutta integration method in the x or χ direction.

III. RESULTS

The formulation and numerical implementation above are now used to study the flow of a thin viscoelastic jet emerging from the channel as illustrated schematically in Fig. 1. Both steady and transient flows are examined. The physical domain of the fluid is assumed to extend from $x = 0$ to $x \to \infty$, but the computational domain will be restricted to $x \in [0, 1]$. The influence of fluid elasticity is investigated at a moderately low Reynolds number in order not to make inertia completely dominant. The interplay amongst inertia, elasticity, and gravity will be emphasized. The flow of a Newtonian fluid is also examined for reference.

A. Steady Newtonian jet flow

The influence of inertia on steady jet flow is first examined for a Newtonian fluid by varying the Reynolds number from Re $\in$ [10, 50] while assuming negligible gravity (Fr $\to \infty$).

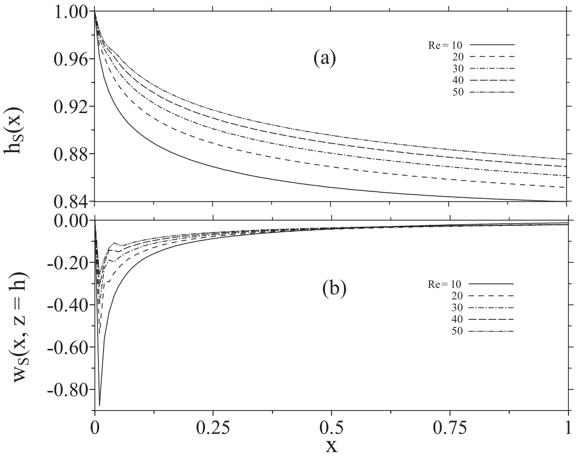

FIG. 2. Influence of inertia on steady-state Newtonian jet thickness (a), and surface transverse velocity (b) in the absence of gravity ($1/\mathrm{Fr} = 0$), for range Re $\in$ [10, 50].

The flow is illustrated in Fig. 2 with the height of the free surface $h_S(x)$ and the transverse velocity at the free surface $w_S(x, z = h)$ plotted against x for a given Reynolds number. Since mass is conserved, the (average) steady streamwise velocity is simply the inverse of the film height, and is therefore not shown. The film profiles in Fig. 2(a) show a monotonic response of the jet thickness, with a strong contraction in film height close to the channel exit. This contraction is weakened by inertia. The curves in the figure suggest, as expected, that for Reynolds number, the jet thickness remains constant with x, with plug-flow conditions reached almost immediately downstream from the channel exit. The contraction in height is accompanied by a sharp drop in transverse velocity [see Fig. 2(b)], which reaches a minimum at a location close to the channel exit that is essentially independent of inertia. Note that plug flow conditions ($h_s \to$ const, $w_s \to 0$) are reached far downstream from the channel exit at any Reynolds number.

Further insight on the role of inertia is inferred from Fig. 3, where the jet thickness is plotted against Re at the location x_m of minimum w_S or maximum downward flow. The flow response is obviously monotonic with respect to Re. The inset in Fig. 3 indicates that $h_S(x_m)$ grows like $3.2 \times 10^{-4} \ln(\mathrm{Re})$. The figure shows that the flow is strongly dependent on inertia for small Reynolds number. In fact, as Re $\to 0$, the jet tends to infinitely contract near $x = 0$, collapsing onto an infinitely thin

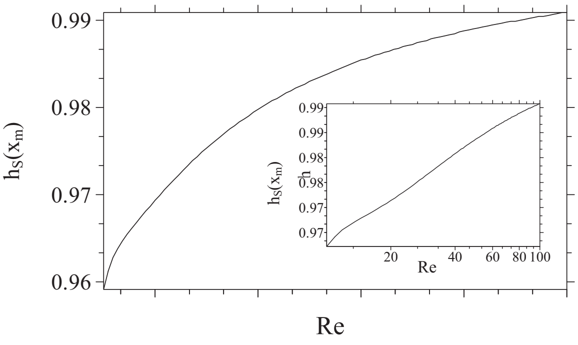

FIG. 3. Jet thickness for a Newtonian jet as function of inertia. (inset shows semilog scale) at the location x_m of minimum.

filament. In this limit, $w_S \to -\infty$ (not shown). This behavior is exactly opposite to that encountered for a wall jet [25–30] (a jet exiting a channel and flowing over a rigid plate as in a coating flow). In that case, the film thickness grows infinitely in the limit $\mathrm{Re} \to 0$, indicating that the film accumulates near the channel exit, resisting flow. This contrast in flow behavior has a dramatic fundamental and practical consequence if one views the flow of the jet film as equivalent to the (slipping) flow of a thin film over a fully lubricated plate. This becomes particularly relevant in the case of polymeric film flow over a flat plate where slippage can occur, and the flow behaves like a symmetric free jet rather than a wall jet. The difference between the two situations originates from the difference in boundary conditions, namely stick as opposed to slip at $z = 0$, and is worth further consideration (see the following).

The formulations for both free and wall jet flows are given in Appendix A. In the absence of inertia ($\mathrm{Re} \to 0$), and if the stick condition is assumed, then the conservation of momentum equation in (A1) along with the dynamic condition in (A3) admit $u_s(x,z) = 0$ as solution for $x > 0$ and $z \in [0,\, 1]$. This leads to a significant elongational effect as the flow is forced to transition from Poiseuille to free jet flow, with $u_{s,x} < 0$ at the channel exit, which in turn induces a correspondingly significant jump in w_S, resulting in $h_{s,x}(x = 0) > 0$ or film expansion according to the kinematic condition in (A3). On the other hand, if the slip condition is used, then the solution to the problem is given by $u_s(x,z) = 1$ for $x > 0$, leading to $u_{s,x} > 0$ and $h_{s,x}(x = 0) < 0$, resulting in film contraction. The difference in flow between free and wall jets is further underlined shortly for viscoelastic jets.

The overall flow is depicted from Fig. 4 for Re = 10. The contours of the stream function (streamlines and flow field) and the streamwise and transverse velocity components are shown in Figs. 4(a)–4(c), respectively. As expected, the flow is predominantly in the streamwise direction with plug-flow conditions prevailing for approximately $x > 0.75$. The strength of transverse flow is essentially confined to the free surface near the channel exit. The strong elongational flow, which is particularly evident near $x = 0$, is accompanied by a strong variation of the transverse flow with z. Note the upward flow near $x = 0$.

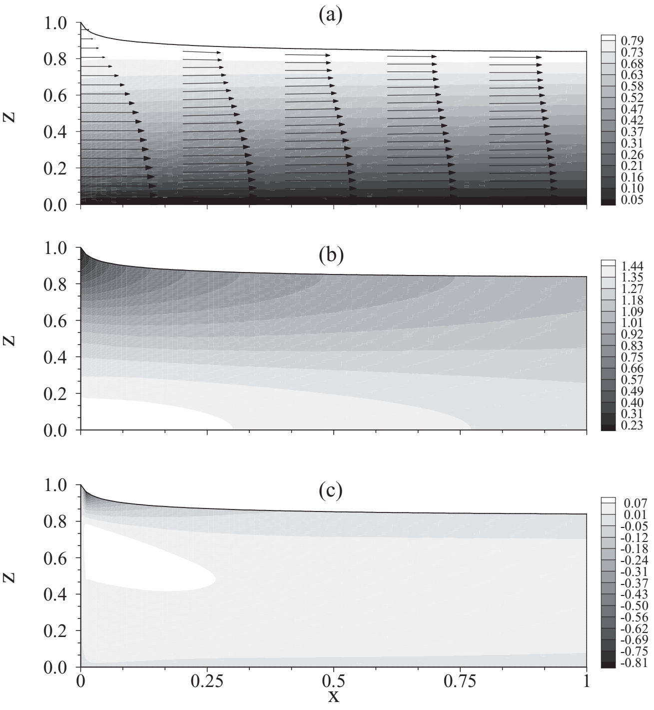

FIG. 4. Flow pattern and velocity distribution (a), streamwise (b), and transverse (c) velocity contours in the absence of gravity ($1/\mathrm{Fr} = 0$) for a Newtonian jet ($\mathrm{Re} = 10$).

Finally, the issue of thickness monotonicity for a Newtonian jet is important, as surface waviness is prohibited in this case. This is in sharp contrast to viscoelastic jet flow, which displays extrema as will be seen shortly. Surface monotonicity is proven in the theorem in Appendix B, which states that for steady Newtonian thin film, an extremum cannot occur at the film surface.

B. Steady viscoelastic jet flow

The effect of elasticity can be examined by varying either the viscosity ratio or the Deborah number. In the current work, only De is varied and Rv is set equal to 1, unless otherwise specified. Figure 5 displays the profiles of the jet surface [Fig. 5(a)] and transverse velocity [Fig. 5(b)] at moderately low Reynolds number (Re = 10) in the absence of gravity. The corresponding profiles of the steady components of the shear stress averaged over the jet thickness, $\langle \tau^s_{xz}(x) \rangle$, and the transverse normal stress at the jet surface, $\tau^s_{zz}(x,z = h)$, are also included in Figs. 5(c) and 5(d), respectively. For $\mathrm{De} < 0.1445$, the flow is qualitatively of Newtonian character. Figure 5(a) shows that elasticity generally enhances the contraction near the channel exit. In contrast to a Newtonian jet, which shows a monotonic decrease in thickness, the viscoelastic jet tends to thicken at a location downstream of the channel exit ($x > 0.125$). The jet thickness [Fig. 5(a)] exhibits a minimum close to the channel exit and a maximum further downstream. As De increases, the location of the minimum becomes closer to $x = 0$, and the location of the maximum shifts further downstream. The jet thickness tends to asymptotically converge to a constant level far downstream from the channel exit. In this case, plug flow conditions are reached regardless of the value of De, similarly to a Newtonian jet [Fig. 2(a)]. Figure 5(b) shows that the w_S profiles reflect a strong downward flow just upstream of the thickness minimum location, exhibiting a minimum at a location that is not strongly affected by elasticity. An overshoot is also observed in w_S similarly to the free surface profile. The waviness, which is typically expected for the flow of viscoelastic films, is more evident here from the w_S than from the h_S profiles. The shear stress in Fig. 5(c) exhibits a minimum and a maximum similarly to the transverse velocity. For low De the shear stress exhibits a mild variation with streamwise position. In contrast, Fig. 5(d) shows a significant buildup in normal stress at the jet surface, with $\tau^s_{zz}(x,z = h)$ reaching a maximum near $x = 0$, coinciding with the minimum in transverse velocity. The buildup level is strongly influenced by elasticity. However, normal stress effect decays with distance to vanish essentially at the same location regardless of the level of elasticity. In comparison, the buildup in shear stress occurs further downstream, with a weak minimum near the exit [Fig. 5(c)]. Generally, Figs. 5(c) and 5(d) indicate that the flow

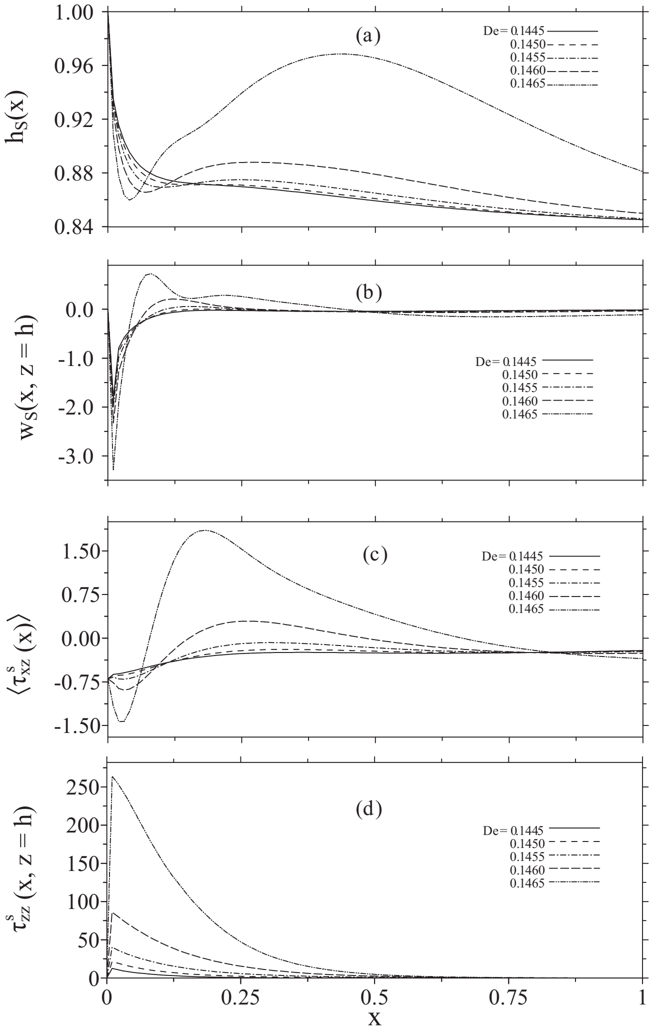

FIG. 5. Influence of elasticity on steady-state jet thickness (a), transverse velocity at the surface (b), average shear stress (c), and transverse normal stress at the surface (d), in the absence of gravity ($1/\mathrm{Fr} = 0$), for De $\in$ [0.1445, 0.1465], Re = 10, and Rv = 1.

is dominated by elongation as opposed to shearing, which is reflected by the large magnitude of $\tau^s_{zz}(x,z = h)$ relatively to that of $\langle\tau^s_{xz}(x)\rangle$. Indeed, even if the scaling for both the normal and shear stress components is taken the same in (2.6b), normal stress effect remains one order of magnitude, $O(\varepsilon^{-1})$, larger. The relative strength of the normal to shear stress components will be examined in detail below.

It is important to note the narrow range of Deborah numbers considered in Fig. 5, De $\in$ [0.1445, 0.1465], reflecting the strong influence of and sensitivity to elasticity. The reason behind the dramatic response for small increments of the Deborah is not intuitively obvious. It is safe to assume that this response has its origin in the nonlinear upper convective terms in the stress equations, and is not likely due to numerical instability since the behavior of flow and stress is qualitatively coherent as De increases. Indeed, the flow kinematics, which is particularly illustrated in Fig. 5(b), suggests that the singularity is strongly enhanced with slight increase in De, as reflected by the deepening of the minimum of the transverse velocity. The increase in the velocity gradient unavoidably entrains the sharp buildup in normal stress. That the severe shearing near the exit is at the origin of the sensitivity of the flow response to elasticity (and inertia—see Fig. 8 below) is further demonstrated by comparing the flows of free and wall jets. Indeed, previous studies by Khayat and co-workers on wall jet flow all indicate that the response is much less sensitive to narrow variations in De [29,30] and Re [25–28]. As demonstrated above, the shear rate near the channel exit is much smaller for a wall jet than for a free jet as the flow retains most of its Poiseuille character upon exiting in the former case. The discontinuity in u at the surface of a wall jet is much stronger for a free jet, making both the elongation rate as well as the shear rate—see Eq. (A5)—sufficiently significant for the dramatic stress response depicted in Figs. 5(c) and 5(d) to occur.

The coherence and accuracy of the trends depicted in Fig. 5 are in agreement with experiment. It is worth exploring the similarity between the current predictions and the experiment of Liang *et al.* [17], although the comparison is limited to the qualitative level. In particular, Liang *et al.* measured the profiles of circular jets. Of close relevance to the current work are the measurements and grey scale images reported in Figs. 2–7 and Figs. 15 and 16 in [17], which depict the influence of the Deborah number on the jet profile issuing from a capillary and an orifice, respectively. Comparison with the predicted profiles in Figs. 5(a) and 6 confirm that a contraction exists near the jet exit, which weakens and approaches the channel (or capillary or orifice) exit as De increases. The development and increase in maximum jet thickness, as well as the position where it occurs, also agree with the trends shown in Figs. 6(a) and 6(b), respectively, from experiment [17]. However, in contrast to experiment, theory suggests that a

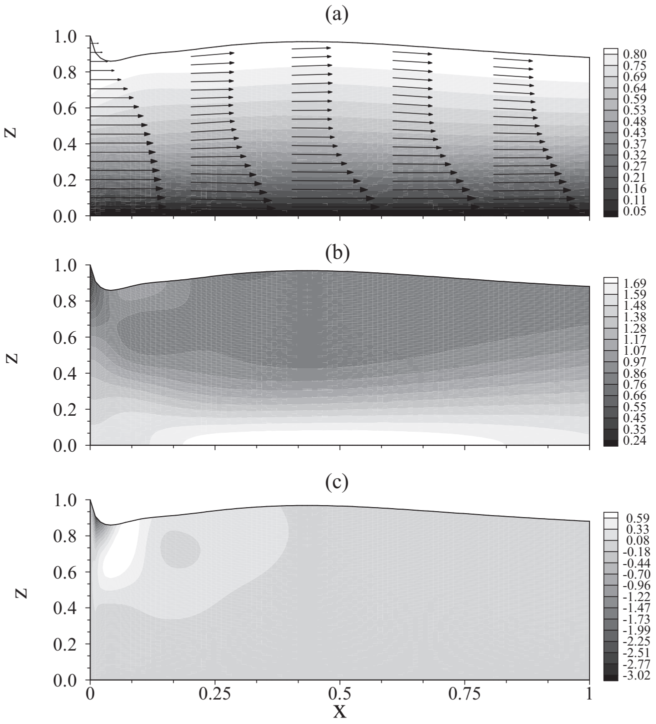

FIG. 6. Flow pattern and velocity distribution (a), streamwise (b), and transverse (c) velocity contours in the absence of gravity ($1/\mathrm{Fr} = 0$) for a viscoelastic jet (De = 0.1465, Re = 10, and Rv = 1).

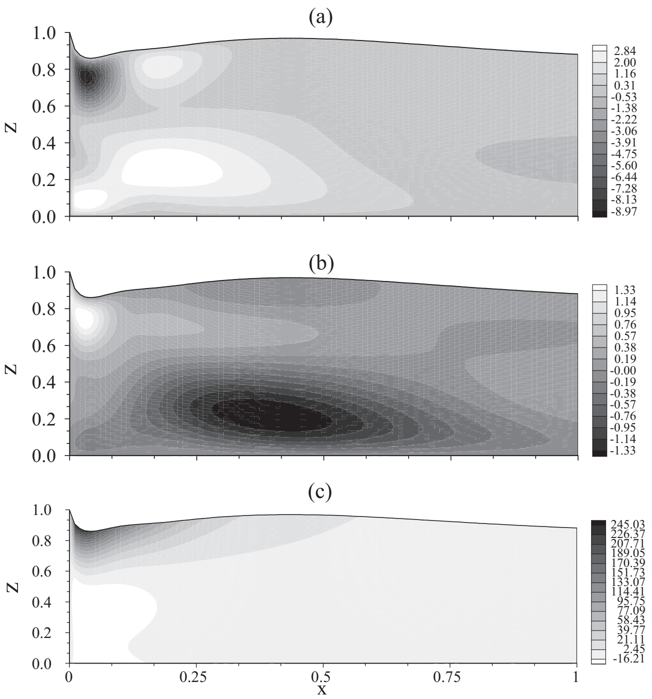

FIG. 7. Contours of polymeric shear stress (a), streamwise (b), and transverse (c) normal stresses in the absence of gravity ($1/\mathrm{Fr} = 0$) for a viscoelastic jet ($\mathrm{De} = 0.1465$, $\mathrm{Re} = 10$, and $\mathrm{Rv} = 1$).

contraction always exists despite its weakening with elasticity. On the one hand, it is possible that experiment eventually fails to capture the existence of a weak contraction, especially as it occurs closer to the capillary or orifice exit. On the other hand, since the origin of the contraction is inertial, one expects a contraction to always exist near the exit given the presence of convection resulting from flow discontinuity.

The onset of waviness in flow variables and jet thickness is obviously the result of elastic effect. Recall that the thickness of a Newtonian jet is always monotonic with position (Appendix B). The nonmonotonicity of a viscoelastic jet is illustrated by taking a perturbation expansion of the stress components and assuming De small. If one examines the stress equations in the vicinity of the free surface, one finds, upon neglecting terms of $O(\mathrm{De}^2)$, that Eqs. (2.8c) and (2.8d) lead to $\tau_{xx} \simeq 2a\mathrm{De}\, u_{,z}^2$ and $\tau_{xz} \simeq a u_{,z}$, respectively. This indicates that τ_{xx} diminishes faster than τ_{xz} as the shear rate decreases upon approach of the free surface. Simultaneously, Eq. (2.8e) indicates that, to leading order, $\tau_{zz} \simeq 2a w_{,z}$. In this case, $w_{,X}$ can be estimated from the higher-order terms, which, together with Eq. (2.10), give

$$h_{,xx} = \frac{w_{,x} - u_{,x}h_{,x}}{u} \simeq -\frac{\frac{uu_{,xx}+2u_{,x}^2}{u_{,z}} + u_{,x}h_{,x}}{u}. \tag{3.1}$$

Consequently, given the small shear rate at the free surface, the curvature reduces to

$$h_{,xx} \simeq -\frac{uu_{,xx} + 2u_{,x}^2}{uu_{,z}}, \tag{3.2}$$

which illustrates clearly the coupling between shearing and elongation, and its influence on the shape of the free surface. Thus, in situations where $u_{,X}$ is large such as close to the channel exit in the vicinity of the free surface, with $u_{,z}$ simultaneously small, $h_{,xx}$ can be large, and an extremum can therefore exist as shown in Fig. 5(a). Expression (3.2) also shows that, given the negative shear rate and positive elongation rate, the concavity is positive, reflecting jet contraction at the channel exit. Interestingly, this seems to be always the case regardless of the elasticity level, even in the presence of die swell.

Figure 6 details the flow kinematics for $\mathrm{De} = 0.1465$, $\mathrm{Re} = 10$, and $\mathrm{Rv} = 1$. The streamlines and flow field are shown in Fig. 6(a), and the streamwise and transverse velocity contours are shown in Figs. 6(b) and 6(c), respectively. A major contrast between the Newtonian and viscoelastic jet flows is reflected in the flow field (compare Figs. 4 and 6). For a Newtonian jet, the flow becomes fully developed and reaches plug flow conditions only far downstream from the channel exit. In contrast, a viscoelastic jet displays uniform flow much closer to the channel exit, over a relatively deep region below the free surface. Thus, while the boundary-layer region extends over the entire jet thickness for a Newtonian jet, it remains confined to the core region for the viscoelastic jet. Moreover, the approximate expression (3.2) for the concavity correlates well with the free surface shape in Fig. 6. More particularly, Fig. 6(b) indicates that, close to the channel exit where the flow is still of Poiseuille character, $u_{,Z} < 0$ in the vicinity of the free surface, leading to the formation of a minimum in accordance with (3.2). Further downstream, where the maximum in h occurs, $u_{,Z} > 0$ between the core region and the free surface. Note, however, that the maximum in this case is relatively weak, and $u_{,Z}$ is only slightly positive. Nevertheless, the fact that $u_{,Z}$ is positive is most evident from Fig. 6(b) just downstream from the free surface depression. Figure 6(c) indicates that the sharp jump and drop in w observed at the free surface [see Fig. 5(b)] extends well below the free surface. The jump and drop occur just downstream of the free surface minimum and maximum, respectively. Note that the jump is much more pronounced than the drop. The corresponding contours for the stress components τ_{xz}^s, τ_{xx}^s, and τ_{zz}^s are depicted in Figs. 7(a)–7(c), respectively. Figure 7 indicates that most of the viscoelastic character is concentrated close to the channel exit where significant elongation and shearing are present. Figure 7(a) indicates the presence of sharp variation in τ_{xz}^s close to the free surface and in the jet core. This is also reflected in Figure 5(c). In particular, a sharp jump $\langle \tau_{xz,x}^s \rangle \gg 0$ is observed just downstream of the surface depression. This jump can be estimated from Eq. (2.8d). First note, however, from Figs. 8(b) and 8(c), that both τ_{xx}^s and τ_{zz}^s are predominantly positive near the free surface, with $\tau_{zz}^s \gg \tau_{xx}^s$. Figure 8 suggests that the dominant terms in Eq. (2.8d) lead to the following estimate for the jump:

$$\tau_{xz,x} \approx \frac{1}{u}(\tau_{xx} w_{,x} + \tau_{zz} u_{,z}). \tag{3.3}$$

Interestingly, both terms on the right-hand side of (3.3) are positive and large. Indeed, Fig. 5 indicates that $w_{,X}$ is positive and large near the depression. Figure 6(a) suggests that $u_{,Z} > 0$ at the same location. Note that although $u_{,Z}$ is not large near the free surface, τ_{zz} is very large as Figs. 5(d) and 7(c) suggest. This buildup in τ_{zz} starts at the channel exit where τ_{xz} is large, and is accompanied by a large drop in w as a result of jet

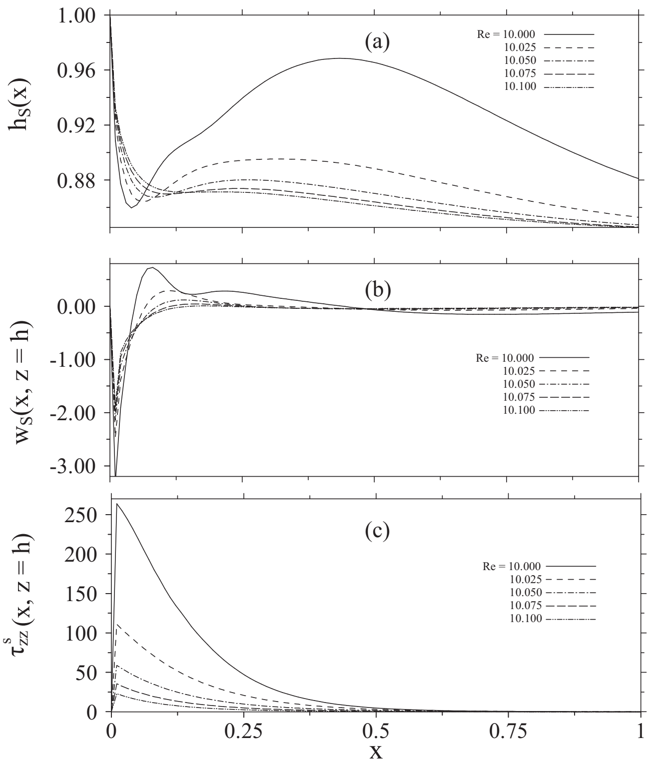

FIG. 8. Influence of inertia on steady-state jet thickness (a), transverse velocity (b), and transverse normal stress (c) at the surface, in the absence of gravity ($1/\text{Fr} = 0$) for a viscoelastic jet for $\text{Re} \in [10, 10.1]$, $\text{De} = 0.1465$, and $\text{Rv} = 1$.

contraction. The streamwise buildup in τ_{zz} close to $x = 0$ can be estimated from the dominant terms in Eq. (2.8e), namely

$$\tau_{zz},_x \approx \frac{2}{u}\tau_{xz}w,_x. \tag{3.4}$$

In particular, there is significant elongational flow in the vicinity of the jet depression, as suggested by the large positive value of τ^s_{zz} [Fig. 5(d)]. This buildup in normal stress effect, which is the result of intense shearing as suggested by (3.4), leads, in turn, to *shock* formation as discussed later.

The interplay between the effects of elasticity and inertia is now examined. The influence of inertia for a relatively highly elastic jet flow is illustrated in Fig. 8. The profiles for $h_S(x)$, $w_S(x,z = h)$ and $\tau^s_{zz}(x,z = h)$ are shown in Figs. 8(a)–8(c), respectively. Here $\text{De} = 0.1465$ and $\text{Rv} = 1$. The flow is strongly influenced by inertia, which explains the narrow range $\text{Re} \in [10,10.1]$ used. The figure indicates that a very small increase in Re has the effect of lowering the free surface maximum to a relatively large degree. In contrast, the minimum level in the free surface does not appear to vary considerably with Re. Overall, the jet profiles, velocity, and normal stress distributions suggest that inertia tends to play an opposite role to elasticity. Figures 5 and 8 indicate that a reduction in inertia level or rise in elasticity level for a viscoelastic jet leads to the emergence of surface waviness and excessive normal stress level. This rise in normal stress leads in turn to the formation of sharp gradients in velocity and shear stress. Thus, at a critical elasticity or inertia level, these gradients can be sufficiently substantial to cause a discontinuity or shock in the flow. Of course, velocity gradients and polymeric stresses are coupled as expressions (3.3) and (3.4) suggest. However, the variation in w_S and the jump in τ^s_{xz} appear to be primarily responsible for shock formation [see Figs. 5(b), 5(c), and 8(b)].

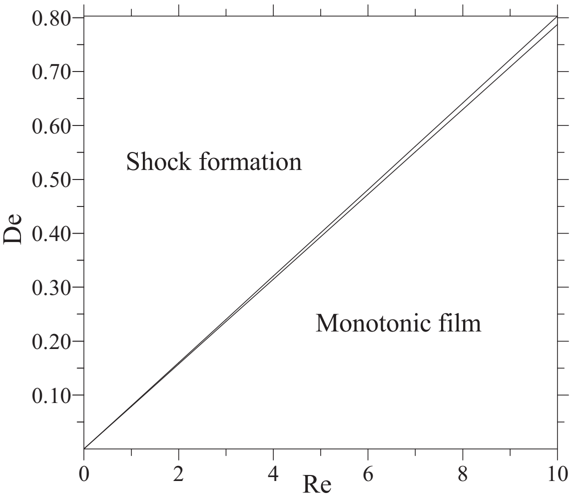

FIG. 9. Dependence of the critical Deborah number on inertia for the onset of waviness and shock in the absence of gravity ($1/\text{Fr} = 0$). Here $\text{Re} \in [0, 10]$, $\text{De} = 0.1465$, and $\text{Rv} = 10$.

Figure 9 depicts the regions of jet waviness and shock formation in the (De-Re) plane for $\text{Rv} = 10$. Interestingly, other Rv values, encompassing most of typical viscosity ratios in practice, seem to give essentially the same picture. For given Re, if De is small, the jet surface decreases monotonically with position. As De increases, the jet surface exhibits waviness. Beyond a critical De value a discontinuity or shock in flow occurs. The two curves bordering the waviness region are straight and intersect at the origin. The intersection at the origin reflects the excessive buildup of normal stress effect for a viscoelastic jet flowing at low Reynolds number. This observation is in close correlation with Fig. 5. The slope of the curves is obviously dependent on the viscosity ratio Rv and, as expected, increases with Rv. This indicates, expectedly, that a more dilute fluid solution must have a more elastic polymeric solute for the jet to become wavy. Interestingly, the range of waviness is very narrow, and does not seem to depend strongly on Rv. This illustrates how rapidly the jet surface evolves from a monotonic to a ruptured film.

The influence of gravity is next examined and is illustrated for a jet flow at $\text{Re} = 10$, $\text{Rv} = 1$, and $\text{De} = 0.1465$. The results are shown in Figs. 10–13. The flow in the absence of gravity ($1/\text{Fr} = 0$) is included for reference. The profiles in Fig. 10(a) indicate that gravity tends to suppress surface waviness, as if the jet is drawn at the downstream end. The extrema in h_S tend to weaken and move downstream. The resulting jet profile under high gravitational effect resembles closely the Newtonian jet profile [compare the profiles for $1/\text{Fr} = 1$ in Figs. 10(a) and 10(b) with those for $\text{Re} = 10$ in Figs. 2(a) and 2(b)]. The minima in h_S [in Fig. 10(a) and w_S [in Fig. 10(b)] tend to generally weaken with gravity. The resemblance between the Newtonian jet and viscoelastic jet under high gravity is only apparent and limited to the jet

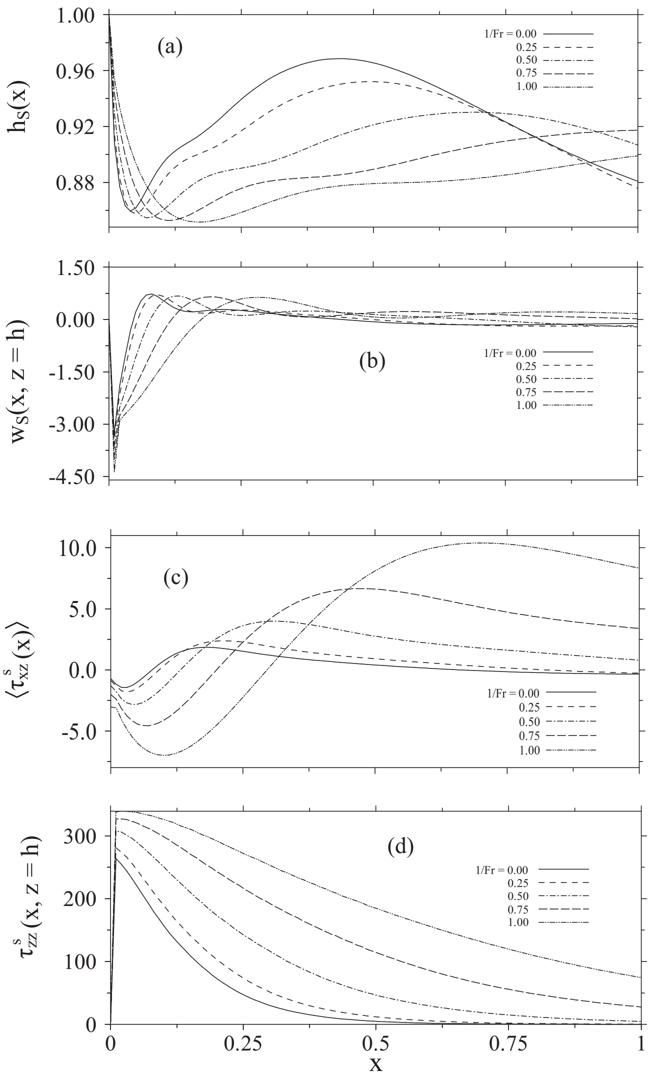

FIG. 10. Influence of gravity on steady-state jet thickness (a), transverse velocity at the surface (b), average shear stress (c), and transverse normal stress at the surface (d), for Fr $\in (\infty, 1]$, Re = 10, De = 0.1465, and Rv = 1.

profile. Indeed, Fig. 10(d) reflects further buildup in normal stress effect as a result of gravity despite the smoothening of the jet profile. This in turn is confirmed from Fig. 10(c), where the jump in the averaged polymeric shear stress is considerably enhanced by gravity. Interestingly, the significant jump in $\langle \tau^s_{xz}(x) \rangle$ is accompanied by only a modest increase in $\tau^s_{zz}(x, z = h)$, which is reflected by the decrease in slope as $1/\mathrm{Fr}$ is increased [see Fig. 10(d)]. Although the jet profiles in Fig. 10(a) seem to suggest that gravity has a stabilizing effect on jet flow, this again is true only in appearance. Figures 11 and 12 show clearly the presence of sharp velocity and stress gradients, which lie beneath an otherwise smooth jet surface. Both shear and elongation effects appear to be spread throughout the jet domain, as opposed to being confined to the region close the channel exit as in Figs. 6 and 7. The enhancement of elastic effect by gravity is also clear from the velocity distributions in Fig. 11(a), which should be compared the velocity profiles in Fig. 4(a) for a Newtonian fluid and Fig. 6(a) for a viscoelastic fluid with no gravity. Interestingly, the minimum u (at some z) is much stronger in the presence of gravity [Fig. 11(a)] than in the absence of gravity [Fig. 6(a)], although the maximum jet thickness is much weaker in this case.

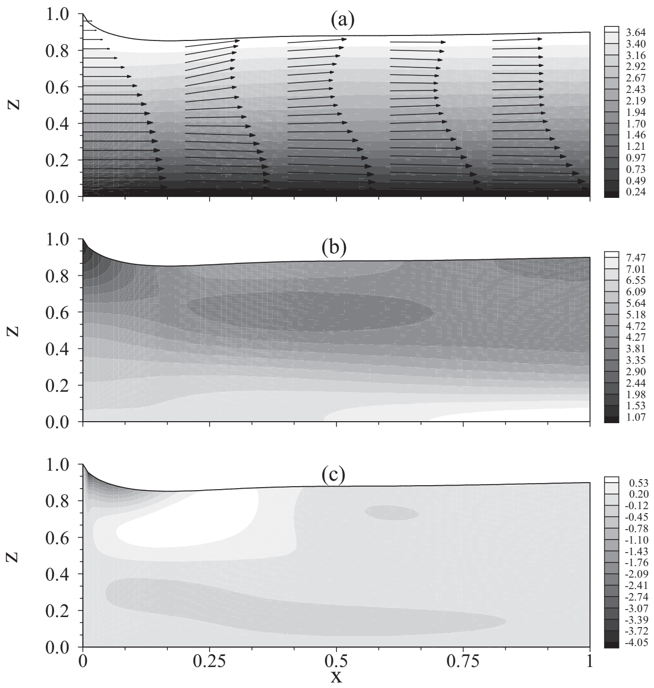

FIG. 11. Flow pattern and velocity distribution (a), streamwise (b), and transverse (c) velocity contours in the presence of gravity for a viscoelastic jet. Here Re = 10, De = 0.1465, Rv = 1, and Fr = 5.

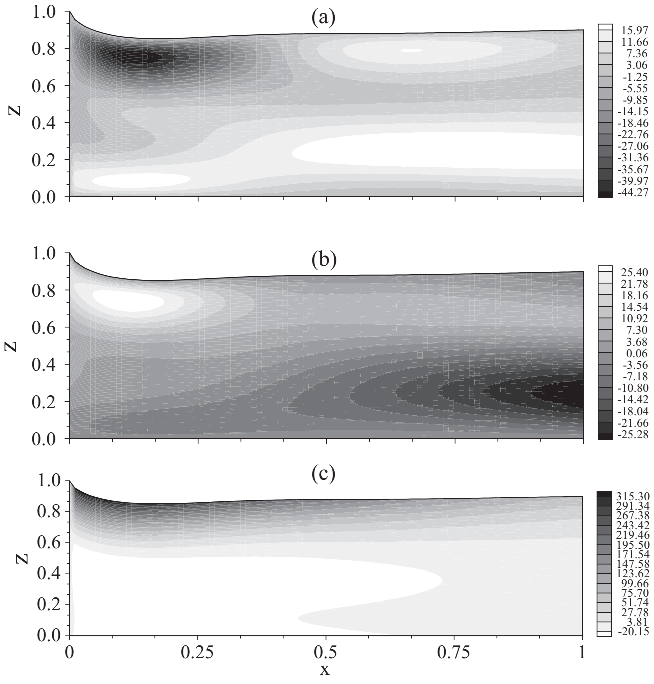

FIG. 12. Contours of polymeric shear stress (a), streamwise (b), and transverse (c) normal stresses in the presence of gravity for a viscoelastic jet. Here Re = 10, De = 0.1465, Rv = 1, and Fr = 4.

C. Transient jet flow

The transient flow response is now examined by considering the evolution of the jet between two steady states, which correspond to two different Reynolds numbers. This would correspond in practice to the situation where, for instance, the flow rate inside the channel is changed from one level to another. One of the major issues concerning viscoelastic flow, in general, is the stability of the steady state. The current nonlinear formulation can shed significant insight on this issue, especially that the calculations can be carried out for large deviation from the steady state whose stability is being examined. Another important issue is the time it takes for the steady state to be reached, assuming it is stable. These issues are addressed systematically below for both Newtonian and viscoelastic jets, in the absence and presence of gravity.

The first transient analysis is conducted for a Newtonian jet. Figure 13 depicts the evolution of the jet as the Reynolds number is increased from 10 to 100. A three-dimensional perspective is shown in Fig. 13(a), where h is plotted against x and t. Figures 13(b) and 13(c) show the projected profiles for h and w. As expected, for a Newtonian fluid, the transition between the two steady states is monotonic. More importantly, the final steady state, corresponding to $\mathrm{Re} = 100$, appears to be stable. Figures 13(b) and 13(c) show that while the contraction in h is weakening with time, the minimum in w is also weakening. It is interesting to note that, while h tends to take a relatively long time to reach the final steady state, w tends towards the final steady state at a much faster rate initially. This rate can be estimated from Eq. (2.10) and Fig. 13(b). Clearly, the rate of change in w at the free surface is given by

$$\begin{aligned} w_{,t}(x,h,t) = h_{,tt}(x,t) + u_{,t}(x,h,t)h_{,x}(x,t) \\ + u(x,h,t)h_{,tx}(x,t). \end{aligned} \tag{3.5}$$

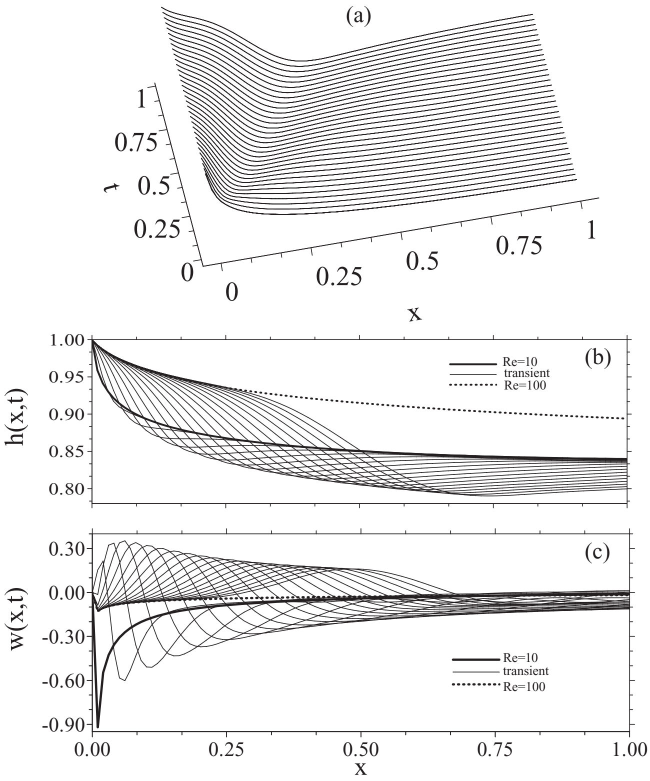

FIG. 13. Transient flow response for a Newtonian jet in the absence of gravity ($1/\mathrm{Fr} = 0$). The figure shows a three-dimensional perspective (a) and a projection (b) of the evolution of the jet thickness, transverse velocity at the free surface (c). The initial and final steady states correspond to $\mathrm{Re} = 10$ and 100, respectively.

Figure 13(b) indicates that $h_{,tt}$ is relatively small and $h_{,x}$ is always negative. In addition, this slow growth in time and small slope in x of h make the second term in Eq. (3.5) dominant. This term is positive since $u_{,t}$ is negative as a result of the expansion of the jet between the initial and final steady states. This leads to $w_{,t}(x,h,t) \approx u_{,t}(x,h,t)h_{,x}(x,t) > 0$ as suggested in Fig. 13(c). It is important to observe from Fig. 13(b) that the transient profiles do not always lie between the two steady states. This would have been the case for diffusive flow of a thick jet, which is governed by parabolic equations (in x). For the present hyperbolic flow, the disturbance starts near the channel exit as the jet attempts to "peel away" from the initial steady state, and is not felt far downstream until much later. The final steady state is reached first near the channel exit. This is expected since, in the absence of gravity, the boundary conditions at $x = 0$ are the same for both initial and final steady states. Finally, additional calculations (not shown) indicate that any steady state for a Newtonian jet appears to be always unconditionally stable regardless of how it is reached. This is not necessarily the case for a viscoelastic jet as will be seen next.

Consider next the transient response for a viscoelastic jet, evolving between the initial and final steady states, corresponding to $\mathrm{Re} = 10$ and 100, respectively. Figure 14 shows the evolution of the flow for $\mathrm{De} = 0.1465$ and $\mathrm{Rv} = 1$, in the absence of gravity, over a time interval $t \in [0,\ 1]$. Figures 14(a) and 14(b) display the surface profiles while Fig. 14(c) depicts the evolution of the average polymeric shear stress. Figures 14(a) and 14(b) show that the transition between the two steady states in this case is smooth, as the jet profile evolves in the form of a traveling wave from the initially highly modulated state (with higher harmonics present) to one that is of harmonic character (with one dominant wave number). It is interesting to note that the amplitude of the h wave remains essentially constant for a relatively long time. In fact, it appears to grow with time in the initial stages. This growth is simultaneously accompanied by an enhanced contraction near $x = 0$, which is a result of the strong downward flow as suggested by Eq. (2.10), and signals a temporary instability of the steady flow at $\mathrm{Re} = 100$. This nonmonotonic dynamic response of $h(x,\ t)$ is even more evident from the evolution of the polymeric shear stress shown in Fig. 14(c). It is interesting to note that the shear stress tends to retain more closely the shape of the initial steady state than the surface profiles. The h-wave amplitude cannot grow indefinitely since the stresses will eventually relax as a result of inertial effect. However, this relaxation process is not uniform. Near the channel exit, for instance, inertia can never be dominant (no matter how large Re is) since inertia is completely absent inside the channel. As a result, there is a slight buildup in shear and normal stresses near $x = 0$. This initial buildup is the result of the intricate coupling in the nonlinear upper-convective terms. Consider

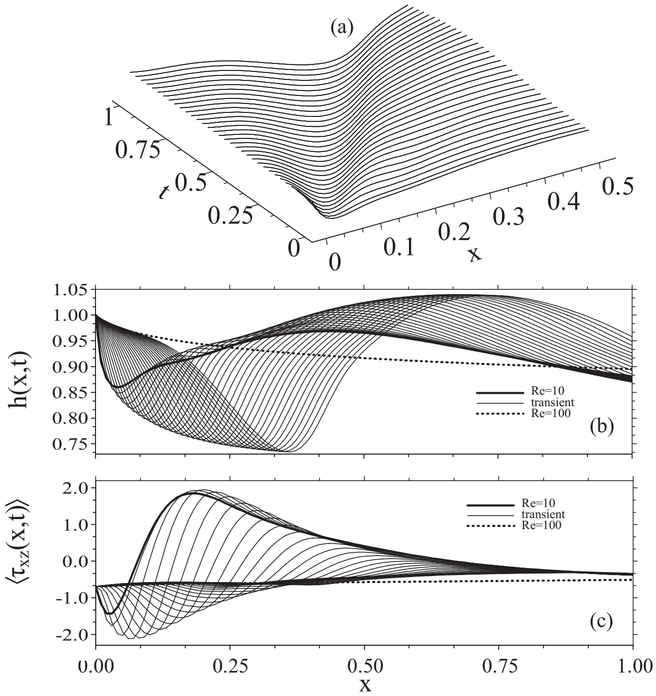

FIG. 14. Transient flow response for a viscoelastic jet in the absence of gravity ($1/\mathrm{Fr} = 0$). The figure shows a three-dimensional perspective (a) and a projection (b) of the evolution of the jet thickness, and average shear stress (c). The initial and final steady states correspond to $\mathrm{Re} = 10$ and 100, respectively. Here $\mathrm{De} = 0.1465$ and $\mathrm{Rv} = 1$.

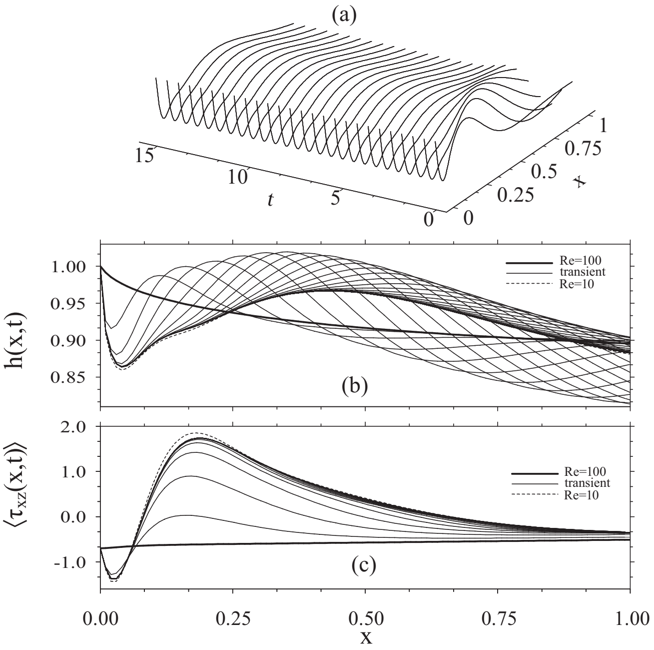

FIG. 15. Transient flow response for a viscoelastic jet in the absence of gravity ($1/\mathrm{Fr} = 0$). The figure shows a three-dimensional perspective (a) and a projection (b) of the evolution of the jet thickness, and average shear stress (c). The initial and final steady states correspond to $\mathrm{Re} = 100$ and 10, respectively. Here $\mathrm{De} = 0.1465$ and $\mathrm{Rv} = 1$.

first the growth in $\langle \tau_{xz}(x,t) \rangle$. It is not difficult to show that the dominant terms in (2.8d) lead to

$$\tau_{xz,t} \approx -u\tau_{xz,x} - w\tau_{xz,z} + \tau_{xx} w,_{x} + \tau_{zz} u,_{z}. \qquad (3.6)$$

Inspection of the steady-state contours and profiles from Figs. 5–8 indicates that only the first term in expression (3.6) is positive. However, this term is weak, especially relative to $\tau_{zz} u,_{z}$. Since the normal stress difference is typically dominated by τ_{zz}, a similar estimate of its growth rate can be obtained from Eq. (2.8e), which gives

$$\tau_{zz,t} \approx -w\tau_{zz,z} - u\tau_{zz,x} + 2\tau_{zz} w,_{z} - \frac{\tau_{zz}}{\mathrm{De}}. \qquad (3.7)$$

However, the estimate (3.7) is not readily conclusive due to the strong competition between the first term on the right-hand side, which is positive near $x = 0$, and the remaining negative terms. Further downstream from the channel exit, the competition is even more intricate. Finally, the stress waves appear to both travel at the same speed, which is relatively slower than that of the h wave. The steady state corresponding to $\mathrm{Re} = 100$ is eventually reached despite its initial (apparent) instability.

The stability of the steady state is an important issue, of fundamental and practical implications. Often, flow instability is encountered in polymer processing. The current problem is naturally relevant to the extrusion of thin films. It is therefore crucial, from a practical perspective at least, to gain further insight into the conditions under which a steady state may or may not be reachable. Figure 14 above clearly indicates the existence of temporary instability as the flow evolves from a highly elastic state to a highly inertial state. Consider next the evolution of the flow in the opposite direction. Figure 15 depicts the transition between the steady flow at $\mathrm{Re} = 100$ to the flow at $\mathrm{Re} = 10$. The rest of the parameters remain the same as in Fig. 14. The jet profile as well as the stresses evolve rather monotonically toward the $\mathrm{Re} = 10$ state. In contrast to the reverse transition, the current transient profiles adhere earlier to the shape of the final steady state (compare the profiles corresponding to $t = 1$ in Figs. 14 and 15). Instead, of a traveling wave, the transition takes the form of a standing wave, which grows essentially in amplitude only. This is most evident from the stress wave in Fig. 15(c). There is strong similarity between the transient profiles and the final steady state at any time. This is again particularly obvious from the stress profiles. It is interesting to observe that the shear stress evolves toward the final state at a much faster rate than the jet free surface, especially near the exit. The w profiles (not shown here) also indicate that the transverse velocity component reaches the final state earlier than h, practically everywhere.

Finally, the transient flow results have been reported so far in the absence of gravity. Figure 16 shows the flow transition between the steady states $\mathrm{Re} = 100$ and $\mathrm{Re} = 10$, with the rest of the parameters remaining the same as in Fig. 15, except that presently $1/\mathrm{Fr} = 0.2$. Comparison between Figs. 15 and 16 indicates that the presence of gravity significantly affects the transition, although the steady states remain qualitatively unaffected. Gravity tends to cause a rapid detachment of the transient flow from the initial steady state ($\mathrm{Re} = 100$) in the early stages, and seems to enhance the already strong contraction initially near $x = 0$. In fact, Figure 16(b) shows that

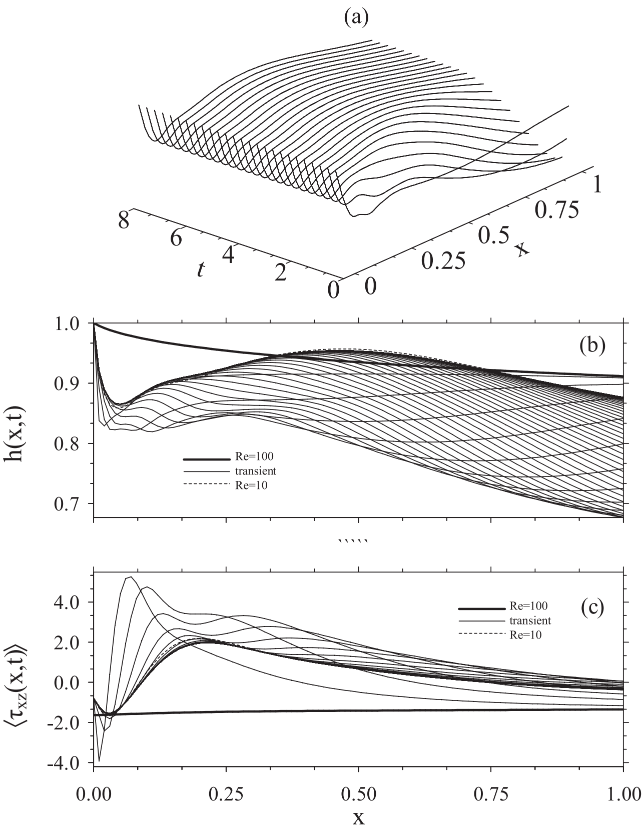

FIG. 16. Transient flow response for a viscoelastic jet in the presence of gravity ($1/\mathrm{Fr} = 0.2$). The figure shows a three-dimensional perspective (a) and a projection (b) of the evolution of the jet thickness, average shear stress (c). The initial and final steady states correspond to $\mathrm{Re} = 100$ and 10, respectively. Here $\mathrm{De} = 0.1465$ and $\mathrm{Rv} = 1$.

all surface profiles approach the $\mathrm{Re} = 10$ state from below. In contrast, in the absence of gravity, the surface profiles tend toward the final steady state from above [see Fig. 15(b)]. The shear stress profiles in Fig. 16(c) indicate a significant stress buildup initially, with normal stress level exceeding significantly the final steady state (not shown). There are strong undershoots and overshoots in stress in the early stages, which tend to subside quickly with time. Therefore, gravity appears to have a strong destabilizing effect on the jet flow initially. Interestingly, however, while the steady state in the absence of gravity is reached essentially at an overall linear rate, the steady state is reached at a rather exponential rate in the presence of gravity despite the early destabilization effect of gravity.

IV. DISCUSSION AND CONCLUDING REMARKS

The current study is limited to planar steady and transient jet flow of a viscoelastic fluid. The problem obviously represents the flow of a thin viscoelastic sheet of infinite span. In reality, this corresponds to the flow of a sheet with span width much larger than its thickness for three-dimensional or edge effects to be significant. It is also assumed that the influence of surface tension is negligible as the current work is focused on the interplay between inertia and elasticity or on the elastico-inertial range. The influence of surface tension tends to weaken for a film with dominant inertia and/or gravity. This has been particularly demonstrated for the flow of Newtonian films. Lee and Mei [36] examined the formation of steady solitary waves on inclined Newtonian thin films, and determined the dependence of the Weber number of different liquids on the Reynolds number for both small and large angles of inclination. They found that surface tension effect decreases strongly with inertia. When cast in terms of the present similarity parameters, the Lee and Mei results show that the capillary number behaves roughly like $\mathrm{Ca} \sim \mathrm{Re}^2/\varepsilon$. This clearly suggests, from (2.8b), that the effect of surface tension is on the order of $\varepsilon^4/\mathrm{Re}^2$. This argument may be extended to include turbulent flow of a thin film [37], or the limit of inviscid flow, such as the formation of tsunamis [38], in which cases, surface-tension effects are clearly negligible. Omodei [39] carried out a two-dimensional finite-element simulation of steady Newtonian jet flow. He found, for example, that the height of the free surface changes by 8% when the capillary number changes from 0.83 to infinity at a Reynolds number (based on channel exit half height) equal to 1, compared to a change in jet thickness of less than 1% when the Reynolds number is greater than 10. A further drop in capillary number is thus required to observe any palpable change in jet height at moderately large Reynolds number. However, further decrease in Ca is not realistic according to experiment. See, for instance, the early study by Goren and Wronski [40] on capillary jet flow. The capillary number can be large for some (essentially) Newtonian fluids with high viscosity, such as the flow of polybutene oils. As an illustration, consider polybutene fluid with mean viscosity, $\mu = 80$ mPa s, density $\rho = 1200\ \mathrm{kg/m}^3$, and surface tension coefficient $\sigma = 50$ mN/m. The film is assumed to move at 12 m/s out of an annulus of 2 mm gap, on a substrate of radius $L = 20$ mm. In this case, $\varepsilon = 0.1$, $\mathrm{Re} = 36$, and $\mathrm{Ca} = 19.2$, making surface-tension effects negligible, and non-negligible inertia. This value of Ca is within the same order of magnitude as those encountered in polymer processing, such as the injection molding of polybutene [41]. Surface tension effect is found to be also negligible for polymeric solution with surface tension coefficient in the range 30–40 mN/m as for the solutions used by Liang *et al.* [17] in their jet flow experiment.

Indeed, surface-tension effect is expected to be even less significant for typical polymeric film flow because of higher viscosity and lower surface-tension coefficient. In jet flow, for instance, polymer solution jets generally take longer to break up than Newtonian jets of comparable (shear) viscosity. Viscoelastic jets may not form droplets at all [42]. Melt fracture occurs essentially in the absence of surface tension for elastic fluids. Even weakly elastic fluids can lead to moderately large capillary numbers, such as 0.5 and 0.75% polyethylene oxides moving at a speed of 10 ms − 1, with $\mathrm{Ca} = 1.2$ and 11, respectively. Strongly elastic polyacrlylamide solutions of 0.1 to 0.75% lead to corresponding Ca value in the range 16–600 [43]. Boger fluids, such as the class of fluids considered in the present study, can also lead to large capillary number flow [44]. For rimming flow, the scaling analysis of Fomin *et al.* [45] also shows that surface-tension effects are negligible in this case.

Finally, it is important to note that surface tension effect can be most significant, and is the (desired) driving mechanism in thin-jet flow, such as the breakup of gas-focused liquid microjets [46,47]. This is even the case for viscoelastic jets where elasticity is shown to enhance jet destabilization [48], thus, fostering the transition from jetting to dripping [49]. However, the influence of surface tension on jet stability may not be consistent, especially for co-flowing liquid jet and gas [50,51].

In conclusion, the symmetric two-dimensional flow of a thin viscoelastic fluid jet emerging from a vertical channel is examined in this study. The fluid is modeled following the Oldroyd-B constitutive model, with the influence of inertia, elasticity, and gravity investigated for both steady and transient flows. The thin-film equations are solved by expanding the flow field and stresses in terms of orthonormal modes in the transverse direction using the Galerkin projection. In contrast to the depth-averaging technique, the proposed method predicts the shape of the free surface, as well as the velocity and stress components within the fluid.

For a steady Newtonian jet the jet thickness remains essentially constant with x for large Reynolds number. However, the flow is strongly dependent on inertia for small Reynolds number with the jet tending to contract and collapse onto a thin line as Re approaches 0. The thickness for a Newtonian jet was shown to vary only monotonically, whereas a viscoelastic jet tends to thicken downstream of the channel exit. Steady Newtonian jet flow becomes fully developed only far downstream from the channel exit. In contrast, a viscoelastic jet displays uniform flow much closer to the channel exit and over a relatively deep region below the free surface. For a steady viscoelastic jet, a reduction in inertia or a rise in elasticity leads to the emergence of surface waviness and excessive normal stress. This rise in normal stress leads to the formation of sharp gradients in the velocity and shear stress. These gradients can be sufficiently substantial to cause a discontinuity or shock in the flow. The wavy region that precedes the onset of shock or jet rupture is very thin, which illustrates how rapidly the jet surface evolves from a monotonic to a ruptured film. High gravity viscoelastic jet flow resembles Newtonian jet flow, but only in appearance and at the free surface. A buildup in normal and shear stress is present for a viscoelastic jet below the surface.

Comparison with the measurements and grey scale images of Liang *et al.* [17] confirms the accuracy of the theoretical trends reported in the current study. Closer comparison between the current theory and experiment is not achievable. While the current model is two dimensional, the experimental jet is round, losing axisymmetry (and stability) with increasing elasticity. In this case, surface tension may be important if the curvature in the plane normal to the jet is significant. The relaxation time and viscosity of the fluid used in the experiment appear to be shear-rate (and temperature) dependent, whereas theory assumes a fluid of constant properties. Also of significance is the assumption of Poiseuille flow condition at the channel exit, which may not be realistic given the developing character of the flow as it nears the exit (see Ref. [20]). Finally, the current predictions are based on a boundary-layer or thin-jet formulation, resulting in additional inaccuracy.

The transient behavior for a Newtonian fluid between two steady states is smooth and appears to be unconditionally stable. However, the transient profiles do not always lie between the two steady states. The flow tends to "peel away" from the initial steady state and is not felt far downstream until much later. The amplitude of the surface height wave for a viscoelastic fluid moving from a low to a high Reynolds number remains essentially constant for a relatively long period of time with growth seen in the initial stages. Both surface and stresses evolve in the form of a traveling wave. This growth is accompanied by an enhanced contraction near the channel exit which is a result of the strong downward flow. This signals a temporary instability of the steady flow, however the final steady state is eventually reached despite this apparent instability. In contrast, for the transition from a high to a low Reynolds number state, the surface profiles adhere earlier to the shape of the final steady state. Instead of a traveling wave, the transition between the two states takes the form of a standing wave, which grows essentially in amplitude only. Finally, the presence of gravity significantly affects the transition between the two steady states, however, the steady states remain qualitatively unaffected. Gravity tends to cause a rapid detachment of the transient flow from the initial steady state in the early stages with a significant stress buildup during the transition.

ACKNOWLEDGMENT

This work was supported by the Natural Sciences and Engineering Research Council of Canada.

APPENDIX A: NEWTONIAN FORMULATION FOR A FREE JET AND A WALL JET

For both thin free and wall jet flows, the relevant equations for Newtonian steady-state flow (in the absence of gravity) are obtained by taking the limit $\mathrm{Rv} \rightarrow \infty$ of Eqs. (2.8), which reduce to:

$$u_{s,x} + w_{s,z} = 0, \quad \mathrm{Re}\,(u u_{s,x} + w u_{s,z}) = u_{s,zz}. \tag{A1}$$

These equations must be solved subject to exit conditions:

$$u_s(x=0,z) = \tfrac{3}{2}(1-z^2), \quad h_s(x=0) = 1, \tag{A2}$$

dynamic and kinematic conditions:

$$u_{s,z}(x,z=h_s) = 0, \quad w_s(x,z=h_s) = u_s(x,z=h_s)h_{s,x}, \tag{A3}$$

and slip or stick condition, depending on whether, respectively, free or wall jet flow is assumed,

$$u_{s,z}(x,z=0) = 0 \quad \text{or} \quad u_s(x,z=0) = 0. \tag{A4}$$

The relation between the shear and elongation rates at the free surface is readily available by differentiating the kinematic condition in (A3), to yield

$$\begin{aligned} w_{s,x}(x,z=h_s) = {} & u_{s,x}(x,z=h_s)h_{s,x}(x) \\ & + u_s(x,z=h_s)h_{s,xx}(x). \end{aligned} \tag{A5}$$

Thus, a strong discontinuity in the streamwise flow, as at the channel exit of a free jet, leads to a significant buildup in shearing flow.

APPENDIX B: MONOTONICITY OF NEWTONIAN FILM

Theorem. For steady Newtonian thin film, an extremum cannot occur in the film thickness.

Proof. If an extremum exists at some location, say x_m, on the free surface of the steady film, with $h_s(x_m) = h_m$, then, according to condition (2.9), $w_s(x_m,h_m) = h_{s,x}(x_m) = 0$. Simultaneously, condition (2.9) leads to the following expression for the concavity:

$$h_{s,xx}(x_m) = \frac{w_{s,x}(x_m,h_m)}{u_s(x_m,h_m)}, \tag{B1}$$

which must not vanish for an extremum to exist. However, upon differentiating the second equation in (A1) with respect to z and evaluating it at the free surface, using conditions (A3), one obtains

$$\mathrm{Re}\, w_s(x,h_s)u_{s,zz}(x,h_s) = u_{s,zzz}(x,h_s). \tag{B2}$$

Clearly, since $w_S(x_m,h_m) = 0$, then $u_{s,zzz}(x_m,h_m) = 0$. On the other hand, differentiating Eq. (B2) with respect to x (along the free surface), and evaluating it at the location of the extremum, one finds that

$$\mathrm{Re}\, w_{s,x}(x_m,h_m)u_{s,zz}(x_m,h_m) = u_{s,zzzx}(x_m,h_m) = 0. \tag{B3}$$

Therefore, $w_{s,x}(x_m,h_m)$ or $u_{s,zz}(x_m,h_m)$ must vanish. However, at the location of an extremum, the conservation of momentum equation in (A1) gives $u_{s,zz}(x_m,h_m) = \mathrm{Re}\, u_s(x_m,h_m)u_{s,x}(x_m,h_m)$. Consequently, $u_{s,zz}(x_m)$ cannot vanish (in the presence of a contraction or an expansion), except for the trivial case of fully developed uniform (plug) flow. In this case, only $w_{s,x}(x_m,h_m)$ must vanish, forcing the concavity to vanish according to (B3). This proves that the thickness can only vary monotonically for Newtonian thin film.

[1] G. J. Donnelly and C. B. Weinberger, Ind. Eng. Chem. Fundam. **14**, 334 (1975).
[2] F. Cao, R. E. Khayat, and J. E. Puskas, Int. J. Solids Struct. **42**, 5734 (2005).
[3] J. C. Slattery and S. Lee, J. Non-Newtonian Fluid Mech. **89**, 273 (2000).
[4] Y. T. Shah and J. R. A. Pearson, Ind. Eng. Chem. Fundam. **11**, 150 (1972).
[5] R. German and R. E. Khayat, Phys. Fluids **17**, 102104 (2005).
[6] B. Seyfzadeh, G. M. Harrison, and C. D. Carlson, Polym. Eng. Sci. **45**, 443 (2005).
[7] A. K. Doufas and A. J. Mchugh, J. Rheol. **45**, 403 (2001).
[8] H.-C. Chang, Ann. Rev. Fluid Mech. **26**, 103 (1994).
[9] C. Berdaudo, A. Fortin, T. Coupez, Y. Demay, B. Vergnes, S. V. Alekseenko, V. E. Nakoryakov, and B. G. Pokusaev, AIChE J. **31**, 1446 (1985).
[10] F. Kang and K. P. Chen, J. Non-Newtonian Fluid Mech. **57**, 243 (1995).
[11] M. F. Tome, B. Duffy, and S. Mckee, J. Non-Newtonian Fluid Mech. **62**, 9 (1996).
[12] Y. Christanti and L. M. Walker, J. Non-Newtonian Fluid Mech. **100**, 9 (2001).
[13] D. W. Bousfield, R. Keunings, G. Marrucci, and M. M. Denn, J. Non-Newtonian Fluid Mech. **21**, 79 (1986).
[14] Y. L. Zhang, O. K. Matar, and R. V. Craster, J. Non-Newtonian Fluid Mech. **105**, 53 (2002).
[15] H. A. Tieu and D. D. Joseph, J. Non-Newtonian Fluid Mech. **13**, 203 (1983).
[16] T. Tran-Cong and N. Phan-Thien, Rheol. Acta. **27**, 639 (1988).
[17] Y. Liang, A. Oztekin, and S. Neti, J. Non-Newtonian Fluid Mech. **81**, 105 (1999).
[18] S. Middleman and J. Gavis, Phys. Fluids **4**, 963 (1961).
[19] M. Cloitre, T. Hall, C. Mata, and D. D. Joseph, J. Non-Newtonian Fluid Mech. **79**, 157 (1998).
[20] A. Saffari and R. E. Khayat, J. Fluid Mech. **639**, 65 (2009).
[21] V. Y. Shkadov, Izv. Akad. Nauk SSSR, Mekh. Zhidk. Gaza **1**, 43 (1967).
[22] E. A. Demekhin and V. Ya. Shkadov, Izv. Akad. Nauk SSSR, Mekh. Zhidk. Gaza **3**, 63 (1985).
[23] O. Takashi, Phys. Fluids **11**, 3247 (1999).
[24] A. L. Frenkel, Europhys. Lett. **18**, 583 (1992).
[25] R. E. Khayat and S. Welke, Phys. Fluids **13**, 355 (2001).
[26] R. E. Khayat and K. Kim, Phys. Fluids. **14**, 4448 (2002).
[27] M. Tauqeer and R. E. Khayat, Phys. Fluids **16**, 1818 (2004).
[28] K. Kim and R. E. Khayat, Phys. Fluids **14**, 2202 (2002).
[29] R. E. Khayat, J. Non-Newtonian Fluid Mech. **95**, 199 (2000).
[30] R. E. Khayat and K. Kim, J. Fluid Mech. **552**, 37 (2006).
[31] R. B. Bird, R. C. Armstrong, and O. Hassanger, *Dynamics of Polymeric Liquids*, 2nd ed. (Wiley, New York, 1987), Vol. 1.
[32] M. Renardy, J. Non-Newtonian Fluid Mech. **68**, 125 (1997).
[33] J. J. Kriegsmann, M. J. Mikis, and J. Vanden-Broek, Phys. Fluids **10**, 1249 (1998).
[34] R. E. Khayat and P. Laure, Int. J. Numer. Methods Fluids **552**, 31 (2012).
[35] O. C. Zienkievicz and J. C. Heinrich, Comput. Methods Appl. Mech. Eng. **17/18**, 673 (1979).
[36] J. Lee and C. C. Mei, J. Fluid Mech. **307**, 191 (1996).
[37] P. K. Stansby and T. Feng, J. Fluid Mech. **529**, 279 (2005).
[38] S. S. Voit, Annu. Rev. Fluid Mech. **19**, 217 (1987).
[39] B. J. Omodei, Comput. Fluids **7**, 79 (1979).
[40] S. L. Goren and S. Wronski, J. Fluid Mech. **25**, 185 (1966).
[41] R. A. Behrens, M. J. Crochet, C. D. Denson, and A. B. Metzner, AIChE J. **33**, 1178 (1987).
[42] M. Goldin, J. Yerushalmi, R. Pfeffer, and R. Shinnar, J. Fluid Mech. **38**, 689 (1969).
[43] S. Middleman, *Fundamental of Polymer Processing* (McGraw-Hill, New York, 1977).
[44] P. C. Huzyak and K. W. Koelling, J. Non-Newtonian Fluid Mech. **71**, 73 (1997).
[45] S. Fomin, T. Hashida, and J. Watterson, J. Non-Newtonian Fluid Mech. **111**, 19 (2003).
[46] A. M. Ganan-Calvo, C. Ferrera, and J. M. Montanero, J. Fluid Mech. **670**, 427 (2011).
[47] J. M. Montanero, M. A. Hamada, E. J. Vega, C. Ferrera, and A. M. Ganan-Calvo, Phys. Fluids **23**, 122103 (2011).
[48] Z. Liu and Z. Liu, J. Fluid Mech. **559**, 451 (2006).
[49] J. M. Montanero and A. M. Ganan-Calvo, J. Fluid Mech. **610**, 649 (2008).
[50] Z. U. Ahmed, R. E. Khayat, P. Maissa, and C. Mathis, Fluid Dyn. Res. **44**, 031401 (2012).
[51] Z. U. Ahmed, R. E. Khayat, P. Maissa, and C. Mathis, Phys. Fluids **25**, 082104 (2013).